

# Mapping Sea Ice Surface Topography in High Fidelity with ICESat-2

Sinéad Farrell<sup>1</sup>, Kyle Duncan<sup>2</sup>, Ellen Buckley<sup>2</sup>, Jacqueline Richter-Menge<sup>3</sup>, and Ruohan Li<sup>2</sup>

<sup>1</sup>University of Maryland College Park

<sup>2</sup>University of Maryland

<sup>3</sup>US Arctic Research Commission & University of Alaska Fairbanks

November 24, 2022

## Abstract

The Advanced Topographic Laser Altimeter System (ATLAS) on ICESat-2 offers a new remote sensing capability to measure complex sea ice surface topography. We demonstrate the retrieval of six sea ice parameters from ICESat-2/ATLAS data: surface roughness, ridge height, ridge frequency, melt pond depth, floe size distribution and lead frequency. Our results establish that these properties can be observed in high fidelity, across broad geographic regions and ice conditions. We resolve features as narrow as 7 m, and achieve a vertical height precision of 0.01 m, representing a significant advance in resolution over previous satellite altimeters. ICESat-2 employs a year-round observation strategy spanning all seasons, across both the Arctic and Southern Oceans. Because of its higher resolution, coupled with the spatial and temporal extent of data acquisition, ICESat-2 observations may be used to investigate time-varying, dynamic and thermodynamic sea ice processes.

# Mapping Sea Ice Surface Topography in High Fidelity with ICESat-2

S. L. Farrell<sup>1</sup>, K. Duncan<sup>2</sup>, E. M. Buckley<sup>3</sup>, J. Richter-Menge<sup>4</sup>, R. Li<sup>1</sup>

<sup>1</sup>Department Geographical Sciences, University of Maryland, College Park, MD, USA.

<sup>2</sup>Earth System Science Interdisciplinary Center, University of Maryland, College Park, MD, USA.

<sup>3</sup>Department of Atmospheric and Oceanic Science, University of Maryland, College Park, MD, USA.

<sup>4</sup>Institute of Northern Engineering, University of Alaska Fairbanks, Fairbanks, AK, USA.

Corresponding author: Sinéad Louise Farrell (sineadf@umd.edu)

## Key Points:

- ICESat-2 provides a new remote sensing capability to measure complex sea ice surface topography at m-scale resolution, across all seasons
- We demonstrate approaches to retrieve six, key sea ice parameters using ICESat-2 laser altimeter height measurements
- ICESat-2 observations may be used to investigate time-varying sea ice processes, advancing forecasting and modelling efforts

25 **Abstract**

26 The Advanced Topographic Laser Altimeter System (ATLAS) on ICESat-2 offers a new remote  
27 sensing capability to measure complex sea ice surface topography. We demonstrate the retrieval  
28 of six sea ice parameters from ICESat-2/ATLAS data: surface roughness, ridge height, ridge  
29 frequency, melt pond depth, floe size distribution and lead frequency. Our results establish that  
30 these properties can be observed in high fidelity, across broad geographic regions and ice  
31 conditions. We resolve features as narrow as 7 m, and achieve a vertical height precision of 0.01  
32 m, representing a significant advance in resolution over previous satellite altimeters. ICESat-2  
33 employs a year-round observation strategy spanning all seasons, across both the Arctic and  
34 Southern Oceans. Because of its higher resolution, coupled with the spatial and temporal extent  
35 of data acquisition, ICESat-2 observations may be used to investigate time-varying, dynamic and  
36 thermodynamic sea ice processes.

37 **Plain Language Summary**

38 The small footprint, high pulse repetition rate and six-beam configuration of the Advanced  
39 Topographic Laser Altimeter System (ATLAS) on ICESat-2 delivers the highest-fidelity  
40 measurements of sea ice surface topography ever obtained from a spaceborne platform. Since  
41 mid-October 2018, ICESat-2 has provided observations throughout the winter growth and  
42 summer melt seasons. We show that ICESat-2 measurements can be used to derive a suite of  
43 important sea ice properties, including surface roughness, pressure ridge height and frequency,  
44 lead frequency and floe size distribution in the Arctic. We also demonstrate the capability to  
45 detect individual melt ponds on multi-year sea ice, marking the first time summer melt features  
46 have been reliably detected from a space-based altimeter. ICESat-2 observations deliver  
47 unprecedented new details of several sea ice properties that will be transformational in  
48 understanding time-varying polar processes, occurring both during the winter and summer  
49 seasons, under a range of ice conditions.

50 **1 Introduction**

51 Observational evidence from multiple data sources demonstrates that significant, and  
52 rapid, changes are occurring in the Arctic climate system (Richter-Menge et al., 2019). As air  
53 temperatures in the Arctic warm at twice the global rate, long-term declines in sea ice extent,

54 age, and volume, and the duration of the winter growth period, have been observed (Perovich et  
55 al., 2019). Arctic sea ice influences global atmospheric patterns (e.g., Francis et al., 2017),  
56 oceanic thermohaline circulation, and, due to its high albedo, regulates the planetary energy  
57 balance (e.g., Curry et al., 1995). Sea ice properties (e.g., concentration, thickness, drift velocity)  
58 and processes (e.g., growth, melt, divergence, convergence) are, however, some of the most  
59 poorly-constrained variables in global climate models; neither their magnitude nor their impact  
60 on future climate projections are well understood (e.g., Turner & Comiso, 2017). High-resolution  
61 satellite measurements offer a practical solution for achieving spatially and temporally complete  
62 monitoring of sea ice in the polar oceans (Shepherd et al., 2018).

63 Satellite altimeters, deployed on ICESat (2003-2009) and CryoSat-2 (2010 – present),  
64 with orbital inclinations designed to observe Earth’s polar regions, have delivered near-continual  
65 winter-time measurements of sea ice topography at the basin scale since 2003 (e.g. Laxon et al.,  
66 2013). These observations have revealed a decline in Arctic sea ice freeboard, thickness and  
67 volume over the last two decades (e.g. Farrell et al., 2009; Laxon et al., 2013), during which time  
68 the ice cover has transitioned from predominantly multiyear to seasonal ice (Perovich et al.,  
69 2019).

70 NASA’s ICESat-2 continues the polar satellite altimetry record, measuring sea ice  
71 elevation to 88° N/S. Since October 14, 2018, ICESat-2 has provided continual observations of  
72 both polar regions, with the exception of the 2019 summer melt season when an observational  
73 gap occurred between June 26 and July 26, 2019 due to a spacecraft anomaly. The data have  
74 been used to track the evolution of sea ice freeboard in winter (e.g., Kwok et al., 2019c). Here we  
75 present a selection of high-fidelity measurements of sea ice surface topography from ICESat-2,  
76 for a variety of Arctic sites. Our goal is to demonstrate ICESat-2’s unique capability to track  
77 individual floes, from which fine-scale sea ice properties may be derived. We show examples  
78 spanning the end of winter (April 2019), through summer melt (June 2019), and fall freeze-up  
79 (September 2019). Results are validated using independent, coincident observations from  
80 airborne lidar and satellite imagery. We discuss how ICESat-2’s remote sensing capabilities over  
81 sea ice will extend the utility of the data beyond fulfillment of the mission science requirement to  
82 measure freeboard (Markus et al., 2017), by enabling more-detailed process studies.

## 83 **2 Data**

84 ICESat-2 operates in a 91-day exact repeat orbit, with 1387 orbits per cycle. Over the  
85 Arctic Ocean, orbit subcycles of 4 and 29 days offer complete, basin-scale coverage. ICESat-2  
86 carries one primary instrument, the Advanced Topographic Laser Altimeter System (ATLAS).  
87 Six ATLAS beams, arranged in three pairs, span approximately 6.6 km in the across-track  
88 direction. Beam locations are defined relative to spacecraft Reference Ground Tracks (RGTs).  
89 We use the convention *tttccss\_gtxy* to identify specific RGTs, where *t* is the RGT number, *c* is  
90 the orbit cycle, *s* is segment number, *gt* indicates “ground track”, *x* is beam number and *y*  
91 indicates either left (*l*) or right (*r*) beam. Controlled pointing to the RGTs began in March 2019.  
92 Here we use the ATLAS Release 003 Level 2 ATL03 product that contains geolocated photon  
93 heights relative to the WGS84 reference ellipsoid (Neumann et al., 2020). Geolocation of  
94 individual photons results in a vertical range accuracy of 0.05 m and a precision better than 0.13  
95 m (Brunt et al., 2019). We also use Release 002 Level 3 ATL07 sea ice surface heights (Kwok et  
96 al., 2019a), derived from ATL03.

97 Retrievals are validated using two independent data sets. Dedicated Operation IceBridge  
98 (OIB) under-flights of ICESat-2 were conducted in April 2019 to obtain high-resolution (2 m)  
99 Airborne Topographic Mapper (ATM) lidar data along ICESat-2 RGTs in the Canada Basin  
100 (Kwok et al., 2019b). Here we present results from April 22, 2019, when near-coincident (< ~38  
101 minutes) ATM data were acquired. We also utilize high-resolution (10 m) visible imagery from  
102 the Sentinel-2 MultiSpectral Instrument (MSI) for validation.

## 103 **3 Fine-scale Sea Ice Properties**

104 ICESat-2’s predecessor ICESat carried an analogue laser altimeter that had a large  
105 footprint (~50 m) with ~172 m spacing between shots, which limited the resolution of sea ice  
106 observations (Farrell et al., 2011). Overlapping ~12 m-diameter ICESat-2/ATLAS footprints (L.  
107 Magruder, pers. comm.), sampled every ~0.7 m along-track, offer a unique opportunity for  
108 adaptive sampling of the surface, at length scales suitable for discriminating discrete sea ice  
109 features. Following previous work using an airborne simulator for ATLAS (Farrell et al., 2015),  
110 we exploit the innovation of photon-counting laser altimetry to map the rough, topographically  
111 complex, sea ice surface at high-resolution. Prior to applying basic sea ice retracking algorithms  
112 to ATL03 photon heights, we preprocess the data to remove background noise. We do this by

113 retaining only photons between the 15<sup>th</sup> and 85<sup>th</sup> percentile of the per shot height distribution.  
114 ATL03 atmospheric, tidal, and geoid corrections are applied to obtain corrected elevation.  
115 Following Duncan et al. (2018) and Farrell et al. (2015), elevation is relative to the local level  
116 ice/water surface.

117 In the following sub-sections, we explore ICESat-2's capabilities to observe signatures of  
118 both sea ice dynamics (ice pack convergence and divergence) and thermodynamics (sea ice  
119 melt/freeze). We include a brief description of the retrieval of six sea ice parameters from  
120 ATL03 data: surface roughness, ridge height, ridge frequency, melt pond depth, floe size  
121 distribution and lead frequency. We then discuss (in Section 4) their utility in sea ice process  
122 studies.

### 123 **3.1 Surface roughness and pressure ridges**

124 Sea ice roughness ( $\sigma_h$ ) provides an indication of both the mechanical deformation history  
125 of the ice cover and snow distribution across the surface. It is also a proxy for ice thickness.  
126 Knowledge of  $\sigma_h$  is required to understand the exchange of turbulent energy between the ice and  
127 atmosphere, and drag-induced ice dynamics (Zwally et al., 2003). Here,  $\sigma_h$  is the standard  
128 deviation of ATL07 surface height within 25 km-long segments. To illustrate ICESat-2's  
129 capability for obtaining  $\sigma_h$  we consider the Arctic Ocean as a whole (Figure 1a), but also  
130 highlight two regions of the ice cover (regions A and B, Figure 1a) with distinct roughness  
131 characteristics. In April 2019, Arctic-wide  $\sigma_h$  averaged 0.18 m (Figure 1b) but showed a spatial  
132 pattern consistent with the known geographic locations of the seasonal ice zone and the more  
133 heavily-deformed multiyear ice cover (Fig. 3 in Perovich et al., 2019). Region A, north of  
134 Borden Island (Figure 1a, spanning 79.5°-83°N, 100°-120°W), contained multiyear ice  $\geq 3$  years  
135 old and had an average  $\sigma_h$  of 0.3 m, while region B (Figure 1a, spanning 76.25°-81°N, 140°-  
136 160°W), an area of seasonal ice in the Beaufort Gyre, was half as rough ( $\sigma_h = 0.15$  m, Figure 1b).

137 Focusing on representative, 1 km-long segments within each region, we apply the  
138 University of Maryland-Ridge Detection Algorithm (UMD-RDA) to the preprocessed (Section  
139 3) ATL03 photon heights. The UMD-RDA retains the 99<sup>th</sup> percentile of the photon height  
140 distribution for a 5-shot aggregate, applied on a per-shot basis so as to retain full along-track  
141 resolution (0.7 m). When applied to ICESat-2 retrievals over sea ice we obtain a surface

142 elevation profile from which individual pressure ridges may be detected. Following previous  
 143 studies (e.g., Duncan et al., 2018) we define a pressure ridge sail as any local maxima occurring  
 144 above 0.6 m. This threshold distinguishes ridges from lower-amplitude surface features (e.g.,  
 145 snow dunes or sastrugi). Local minima lying above the threshold height are also flagged. Ridge  
 146 width is the along-track distance between minima, or the point(/s) at which elevation drops  
 147 below the threshold height, whichever is closer to the local maxima. Maxima separated by  $\leq 10$   
 148 m are not considered unique and are instead counted as a single ridge (e.g. ridge 8, Figure 1c).

149 Results from the UMD-RDA reveal an average sail height ( $h_s$ ) of 1.5 m for 9 ridges  
 150 spanning 10.7 – 51.8 m in width in region A (Figure 1c). Coincident OIB ATM elevations show  
 151  $h_s$  averaged 1.6 m, verifying the ICESat-2 UMD-RDA result. The altimeter height comparison,  
 152 as well as insight from OIB imagery (Figure 1d), confirms both the location and number ( $n_r$ ) of  
 153 distinct ridges. The ATL07 surface height algorithm accurately detects individual deformation  
 154 features in this region of multiyear ice, however  $h_s$  is underestimated by 0.4 m (0.3 m) when  
 155 compared with ATM (UMD-RDA) (Figure 1c). The results from region A contrast with the  
 156 UMD-RDA statistics obtained over the smoother surface topography of region B. Here,  $h_s$   
 157 averaged 0.8 m for  $n_r = 5$ , ranging 7.1 – 35.7 m in width (Figure 1e). In this area the ATL07  
 158 dataset performs poorly, enabling the detection of only one ridge, with  $h_s = 0.61$  m, suggesting  
 159 surface roughness on seasonal ice may be underestimated by the ATL07 algorithm.

160 Regions A and B contain approximately the same number of 1-km segments ( $n_{seg}$ , Figure  
 161 1f), derived from between 64 and 78 RGTs in April 2019. Aggregating these measurements  
 162 illustrates distinctions in the number of ridges ( $n_r$ ) and their frequency ( $f_r$ , Figure 1f), and in  $h_s$   
 163 (Figure 1g), as a function of ice type. The rougher, older ice in region A was more heavily  
 164 deformed than the ice in region B, with  $\sim 2.5$  times more ridges, that were, on average, 0.28 m  
 165 (0.25 m) taller in mean (modal)  $h_s$ . We found that the 99<sup>th</sup> percentile of sail height ( $h_{s,99}$ ) was  
 166 0.67 m larger in region A than in region B. These results are consistent with an earlier study  
 167 (Duncan et al., 2020) that found  $h_{s,99}$  is a strong indicator of the predominant ice type in which a  
 168 pressure ridge forms.

### 169 **3.2 Melt ponds**

170 Following the end of winter, as air temperatures warm, both thermodynamic and dynamic  
 171 processes introduce meltwater to the system. The presence of low-albedo ponds on the sea ice

172 surface enhances the ice-albedo feedback by increasing absorption of shortwave radiation,  
173 altering Earth's energy budget (Curry et al., 1995). The detection of melt ponds with spaceborne  
174 sensors has proved challenging since ponds are radiometrically similar to open water/leads and  
175 cover small areas ( $\sim 5 - 100 \text{ m}^2$ , Perovich et al., 2002). Early ICESat-2 observations  
176 demonstrated an unexpected capability to penetrate shallow, low turbidity water to measure  
177 coastal bathymetry and identify glacial melt ponds on Antarctic ice shelves (Magruder et al.,  
178 2019; Parrish et al., 2019). These early results, coupled with ICESat-2's high resolution, suggest  
179 the possibility of measuring sea ice melt pond depth and motivate the following analysis.

180 We examine ten, 1 km-long ATL03 segments (Figure 2a, gray dots) acquired along  
181 RGTs crossing the Lincoln Sea (region C, Figure 1a) during the period June 17-22, 2019. Ice in  
182 this region was very rough (Figure 1a) and comprised mainly multiyear floes  $\geq 3.5 \text{ m}$  thick (Fig.  
183 5 in Perovich et al., 2019). The evolution of melt in the Lincoln Sea in 2019 was consistent with  
184 field observations (e.g., Perovich & Polashenski, 2012). The Sentinel-2 MSI time series for the  
185 region (not shown) confirms that surface snow melt was underway by 28 May, and pond  
186 coverage was widespread by 13 June accompanied by a significant drop in surface albedo.  
187 Sentinel-2 imagery of the region on June 22, 2019 (Figure 2b), acquired 37 minutes prior to  
188 ICESat-2 RGT 13070304, confirms the presence of melt ponds on the sea ice surface.

189 Following Buckley et al. (2020), we classified open water, ponded surfaces, and ice floes  
190 in the Sentinel-2 scene (Figure 2b) and used this to validate the presence of ponds in the ICESat-  
191 2 data. By tracking the movement of 10 floes between two overlapping Sentinel-2 images  
192 acquired 50 minutes apart (not shown), we estimated an average ice drift rate of  $9.3 \text{ cms}^{-1}$ . To  
193 account for the time elapsed between the Sentinel-2 and ICESat-2 acquisitions, we applied a drift  
194 correction of 206 m to the imagery. This provided the exact geolocation of melt features in the  
195 Sentinel-2 scene at the time of the ICESat-2 overpass. Assessment of the ICESat-2 segments  
196 (Figure 2a) reveals strong surface returns from the approximately level sea ice surface and  
197 classic concave pond features (Perovich et al., 2003). The latter are a result of ICESat-2 returns  
198 from melt pond bottoms (MP1-10, Figure 2a). Four ponds (MP7-10) can be identified in both the  
199 Sentinel-2 (Figure 2b, insets) and ICESat-2 data (Figure 2a).

200 The small-scale pond features, ranging  $\sim 60 - 280 \text{ m}$  wide (Figure 2a), are not captured by  
201 higher-level ICESat-2 products, such as ATL07 (Figure 2a, cyan). Hence, we developed the

202 University of Maryland-Melt Pond Algorithm (UMD-MPA) to identify pond surfaces (Figure 2a,  
203 black) and bathymetry (Figure 2a, magenta) in the ATL03 data. To determine pond depth ( $h_{mp}$ ),  
204 the algorithm utilizes a two-dimensional histogram with 10 m along-track and 0.1 m vertical  
205 resolution. Pond surface elevation is defined by the mode closest to mean segment elevation.  
206 Ponds occur where a secondary mode in the elevation distribution exists below the surface mode  
207 (e.g. see MP2, Figure 2a). The leading edge of the secondary mode defines pond bathymetry  
208 since this represents the first photon returns from the pond bottom. Its selection mitigates the  
209 impact of photons with delayed arrival times at the detector. Initially,  $h_{mp}$  is derived by  
210 subtracting bottom elevations from pond surface elevation. We note, however, that photon  
211 heights for photons returned from within ponds are not inherently corrected for the refraction of  
212 light at the air-water interface. Therefore, following Parrish et al. (2019, and references therein),  
213 we apply a refraction correction wherein estimated pond depth is scaled by 0.749, the ratio of the  
214 refractive index of air (1.00029) to water (1.33567). After correcting for refraction and linearly  
215 interpolating at 5 m along-track resolution, the  $h_{mp}$  distribution for MP1-10 indicates that  $h_{mp}$   
216 ranged 0.04 – 2.4 m, with a modal (mean) depth of 0.35 m (0.80 m) (Figure 2c). 75% of the  $h_{mp}$   
217 retrievals were  $\leq 1.1$  m. MP9 (inset, Figure 2b), an approximately circular pond, is likely  
218 younger than the other geometrically more complex ponds (Perovich et al., 2002). Combining  
219 maximum  $h_{mp}$  (1.73 m, Figure 2a) with Sentinel-2 pond area (37,000 m<sup>2</sup>, Figure 2b), and  
220 assuming pond volume is approximated by the volume of a spherical cap, we estimate that MP9  
221 contains  $\sim 32,000$  m<sup>3</sup> of melt water.

222 The ICESat-2-derived estimates of maximum  $h_{mp}$  are deeper than those typically  
223 observed in the field (e.g., Perovich et al., 2003). Pond depths can, however, be explained by  
224 their geographical setting on rough multiyear ice and the atmospheric conditions under which the  
225 ponds formed. Regional temperatures in May 2019 were  $\sim 4$ -6 °C above average (Vose et al.,  
226 2014) allowing for enhanced snow melt and mature pond evolution. Sophisticated simulations of  
227 pond evolution (Scott & Feltham, 2010) have suggested that rapid pond deepening, of over 0.5 m

228 in 10 days, can occur on thick, rough multiyear ice, with mean pond depth reaching 0.85 m, in  
229 line with the observations shown here.

### 230 **3.3 Floe size distribution and lead frequency**

231 As the melt season progresses mechanical breakup continues and the unconsolidated ice  
232 pack comprises discrete floes in free drift. Open water fraction increases rapidly, amplified by  
233 lateral melt, and floe size decreases. Solar heat input to the upper ocean increases, further  
234 enhancing melt (Perovich & Richter-Menge, 2015). Lead and floe size statistics, and their  
235 temporal and regional variability, are needed to understand ice-ocean-atmosphere heat fluxes in  
236 summer. Previously, satellite altimeters faced challenges observing summer ice processes.  
237 ICESat operated in campaign mode and did not obtain summer data (Farrell et al., 2009), while  
238 CryoSat-2 has limited along-track resolution (~300 m) and cannot distinguish between summer  
239 melt features (ponds and leads) on the basis of radar altimeter return power, since the radar  
240 backscatter coefficient of sea ice is sensitive to meltwater (Wingham et al., 2006).

241 Here, we revisit the ice cover at the onset of fall freeze-up, focusing on ICESat-2  
242 observations in the Canada Basin (region D, Figure 1a) in early September. Floes in the region  
243 range 10s to 10,000s meters wide (Figure 3a) and are surrounded by thin nilas (WMO, 1970).  
244 Applying the UMD-RDA to a 200 km-long ICESat-2 transect we obtain surface elevation  
245 profiles for the three strong beams. Aggregating heights from ten short (~1 km-long) segments at  
246 locations along the beams (cyan diamonds, Figure 3a) we obtain a zero-mean elevation  
247 distribution with a standard deviation of 0.009 m (blue curve, Figure 3b), illustrating the vertical  
248 height precision of ATLAS over leads. This is a 50% improvement in capability compared with  
249 ICESat, which had a demonstrated precision of ~0.02 m over leads (Kwok et al., 2004). We note  
250 that while the major mode of the ATL07 height distribution for the same leads is consistent with  
251 the UMD-RDA results (gray curve, Figure 3b), 23% of the data fall into a secondary mode, with  
252 a mean elevation of 0.05 m. The reason for this secondary mode is currently unknown, but its  
253 impact is a positive bias in ATL07 sea surface heights.

254 To demonstrate ICESat-2's ability to discriminate individual floes we examine a shorter  
255 (~7.5 km) representative area. In this region, we compare ICESat-2 elevations with a coincident  
256 Sentinel-2 image acquired just 11 minutes after the ICESat-2 pass (Figure 3c). The imagery  
257 reveals nilas between floes of varying sizes, with some evidence of finger rafting. The ICESat-2

258 lead/floe locations, and deviations in their elevation, accurately correspond with the local ice  
259 conditions revealed in the Sentinel-2 MSI data. The ICESat-2 retrievals demonstrate level  
260 elevations across the refrozen lead surfaces and floes ranging 20 m to 3.034 km wide. ICESat-2  
261 modal freeboard, computed at the floe scale, ranged 0.05 m to 1.35 m (Figure 3c). If we suppose  
262 that the floes are in hydrostatic equilibrium with an ice density of  $880 \text{ kgm}^{-3}$  and that a thin  
263 ( $\sim 0.05 \text{ m}$ ), low density ( $\sim 220 \text{ kgm}^{-3}$ ) dusting of snow has accumulated on these floes, we can  
264 estimate an average ice thickness of 2.85 m, which is reasonable when compared with ice mass  
265 balance estimates (Perovich & Richter-Menge, 2015).

266 We extend the analysis to  $\sim 600 \text{ km}$  by combining ICESat-2 retrievals from the three  
267 strong beams and compute lead and floe statistics. Because of the orientation of the track with  
268 respect to the floes (Figure 3a), we do not strictly measure lead width or floe diameter. But, due  
269 to  $>600 \text{ km}$  sample size, the statistics are regionally and seasonally representative. Classifying  
270 open water and ice floes in the Sentinel-2 scene (following Buckley et al., 2020), we tagged lead  
271 and floe pixels along the ICESat-2 track and used these for validation. Based on the results in  
272 Figure 3b, leads are identified in the ICESat-2 data as level ice surfaces with  $\geq 15$  contiguous  
273 retrievals ( $\sim 10 \text{ m}$  along-track width) within 0.1 m of local sea level with a standard deviation of  
274  $\leq 0.01 \text{ m}$ . Lead retrievals accounted for 27.6 % of the ICESat-2 data, which is consistent with a  
275 regional open water fraction of 25.1% derived from Sentinel-2. ICESat-2 retrievals indicate 0-2  
276 distinct leads per kilometer, with an average lead frequency of  $1.3 \text{ km}^{-1}$ , in close agreement with  
277 Sentinel-2 (Figure 3d). While leads ranged 10 m to  $> 3 \text{ km}$ , average (median) lead width was 235  
278 m (71 m), and 75% of leads were  $< 200 \text{ m}$  wide (Figure 3e). Floes, on the other hand, averaged  
279 479 m and 75% were  $< 600 \text{ m}$  wide (Figure 3f). Floe and lead widths differed by 0-14 m between  
280 the two independent estimates (Figures 3e, 3f), demonstrating the quality of the altimeter-derived  
281 metrics. Moreover, the ICESat-2 statistics are consistent with recent studies wherein high-  
282 resolution optical and SAR imagery revealed summer ice floe diameters ranging 10s to 1000s  
283 meters, and averaging  $< 200 \text{ m}$  wide (Arntsen et al., 2015; Hwang et al., 2017).

#### 284 **4 Discussion**

285 The evidence provided here establishes that the small footprint and high pulse repetition  
286 frequency (10 kHz) of ATLAS on ICESat-2 is capable of resolving individual floes, sails and  
287 ponds on the sea ice cover. ICESat-2 retrievals deliver unprecedented quality in the measurement

288 of sea ice properties including floe size distribution, lead frequency, and sail height and  
289 frequency. They also offer the new capability to measure sea ice melt pond depth, derived from  
290 pond bathymetry, the first such measurements to be retrieved using spaceborne altimetry. We  
291 have shown that sea ice surface features as narrow as 7.1 m may be detected. ICESat-2's  
292 capability to retrieve fine-scale sea ice properties year-round will be transformational in  
293 understanding time-varying sea ice processes, and will advance interpretation of lower-resolution  
294 remote sensing data. Evaluating the skill of sea ice process models has been heretofore hindered  
295 by a lack of high-resolution observations covering large spatial and temporal scales (Roach et al.,  
296 2018). The ICESat-2 observation strategy will also address this need.

297 By applying customized surface re-tracking algorithms to ATL03 photon heights we  
298 captured signatures of dynamic ice convergence (pressure ridges) and divergence (leads), and  
299 evidence of summer melt (a thermodynamic process). Our examples show that over level  
300 surfaces, such as recently refrozen leads, an elevation precision of 0.01 m can be achieved,  
301 representing a considerable advance over ICESat. Discrimination of leads, and accurate  
302 measurement of their height, is critical for remote retrieval of sea ice freeboard and thickness  
303 using altimeter techniques, because lead elevation approximates local sea surface height and thus  
304 provides a reference level from which freeboard can be derived (Farrell et al., 2009). Here we  
305 have demonstrated that floe-scale freeboard may be retrieved with ICESat-2. Statistical analysis  
306 of individual floes, and their freeboard, will inform algorithm development for current and future  
307 satellite altimeter missions. Furthermore, the joint sea ice floe size thickness distribution (FSTD)  
308 is required to understand the impact of a geometrical sampling error, an error of omission in  
309 lower-resolution radar altimeter retrievals (Envisat, CryoSat-2) over sea ice (Wingham et al.,  
310 2006). Quantifying this error is critical when combining estimates of sea ice thickness from  
311 multiple altimetric sensors with varying resolutions.

312 High-resolution observations from ICESat-2, such as those shown here, will fill a gap in  
313 knowledge required to advance sea ice modelling (Horvat & Tziperman, 2017). For example,  
314 ICESat-2 measurements of ice pack growth in winter compliment those obtained by CryoSat-2  
315 and will enable investigations of both dynamic and thermodynamic thickening. Routine retrieval  
316 of surface roughness, lead frequency and the FSTD will help advance drag-parameterization in  
317 the next generation of sea ice models. Observing sea ice evolution during summer melt and fall  
318 freeze-up will also improve our understanding of thermodynamically-driven mass loss (Perovich

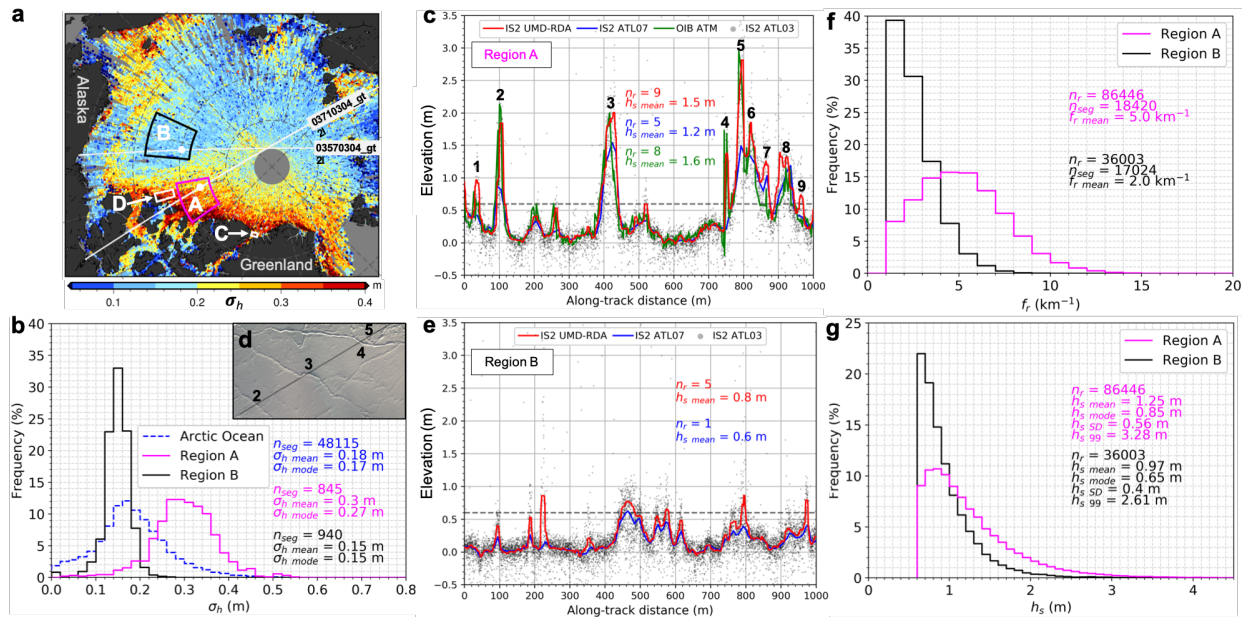
319 & Richter-Menge, 2015). Extending the present analysis of melt ponds to determine regional  
320 variability in pond depth and volume, and their temporal evolution, will be useful for assessing  
321 current parameterizations in melt pond models (Hunke et al., 2013). We note that the spatial  
322 coverage of Sentinel-2 images across the Arctic Ocean (limited by orbit inclination, cloud  
323 interference, and crossover timing with ICESat-2) restricts the extension of the present approach  
324 to estimate pond volume at the Arctic Ocean scale. The potential exists however to estimate  
325 surface topography, melt pond depth and ice thickness simultaneously, with ICESat-2 data alone.  
326 This may be helpful in further constraining our understanding of ice albedo evolution during  
327 summer (Eicken et al., 2004). Tracking both dynamic and thermodynamic processes with  
328 ICESat-2, across a more comprehensive range of sea ice conditions, and seasons, than was  
329 heretofore possible with remote sensing techniques, will also permit examination of ice-ocean-  
330 atmosphere exchanges of energy, mass and momentum, supporting improved understanding of  
331 the connections between sea ice variability and climate forcings.

### 332 **Acknowledgments**

333 This study is supported under NASA Cryosphere Program Grants NNX15AE14G and  
334 80NSSC17K0006. We thank the ICESat-2 science team and project science office for processing  
335 data used in this study, and J. M. Kuhn for assistance with altimetry data processing techniques.  
336 ICESat-2 data are available online from NSIDC (<https://nsidc.org/data/icesat-2>). ATM data are  
337 available at (<https://nsidc.org/data/ilatm1b>). Sentinel-2 MSI imagery are available at:  
338 <https://scihub.copernicus.eu/dhus/#/home>. Temperature data available from NOAA/ESRL  
339 Physical Sciences Laboratory at <https://www.psd.noaa.gov/>.

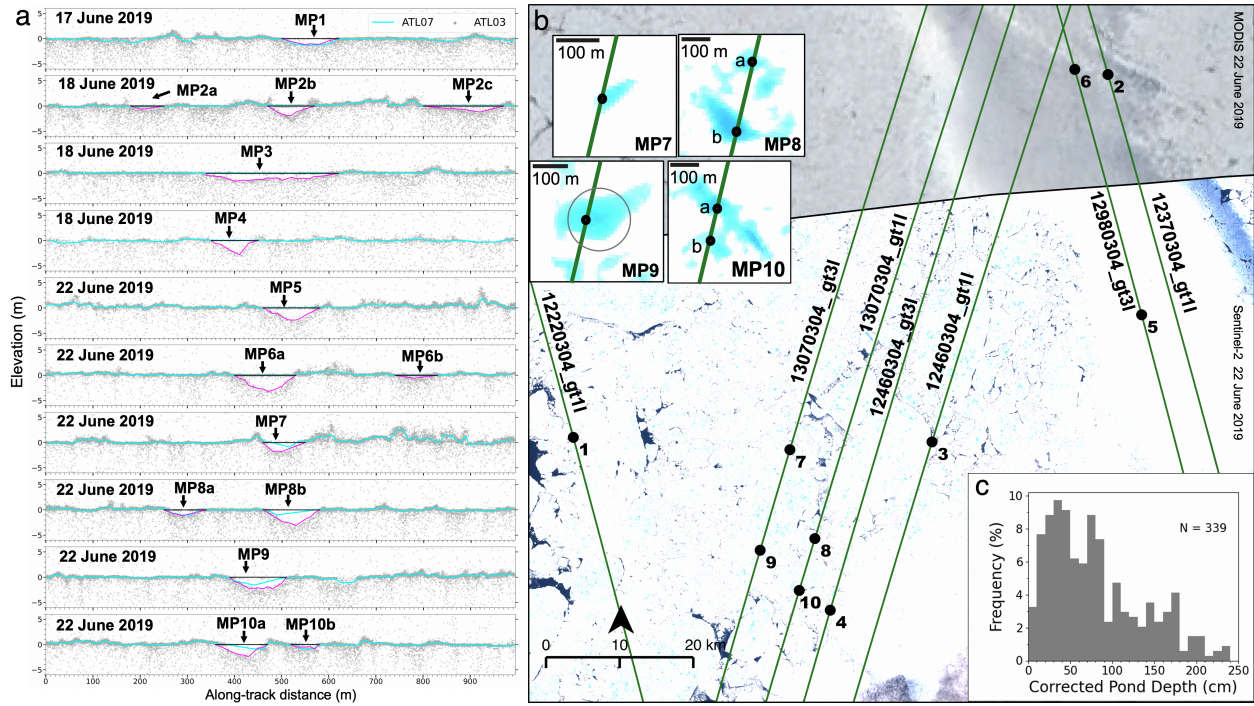
340

341 **Figures**



342  
 343 **Figure 1.** Arctic sea ice roughness and pressure ridge characteristics prior to melt. (a) Ice surface  
 344 roughness ( $\sigma_h$ ) in April 2019 derived from ICESat-2 ATL07, mapped at  $1/8^\circ$ . Regions marked  
 345 A-D are sites of detailed analyses described in the text. (b) Distributions of  $\sigma_h$  for the Arctic  
 346 Ocean (blue dashed line) and regions A (magenta line) and B (black line), as outlined in (a). (c) 1  
 347 km-long transect of sea ice elevation within region A (at white dot) on 22 April, 2019, derived  
 348 from the UMD-RDA (red line), ATL07 (blue line) and ATL03 (gray dots) ICESat-2 products,  
 349 and OIB ATM lidar data (green line). Distinct ridge sails are numbered. (d) Coincident OIB  
 350 image of Region A transect, where numbered features correspond to sails detected in (c). (e)  
 351 Same as in (c) but for transect in region B (at white dot). Note, coincident OIB data were not  
 352 acquired for this transect. (f) Ridge frequency ( $f_r$ ) in regions A (magenta line) and B (black line).  
 353 (g) Same as in (f) but for sail height ( $h_s$ ).

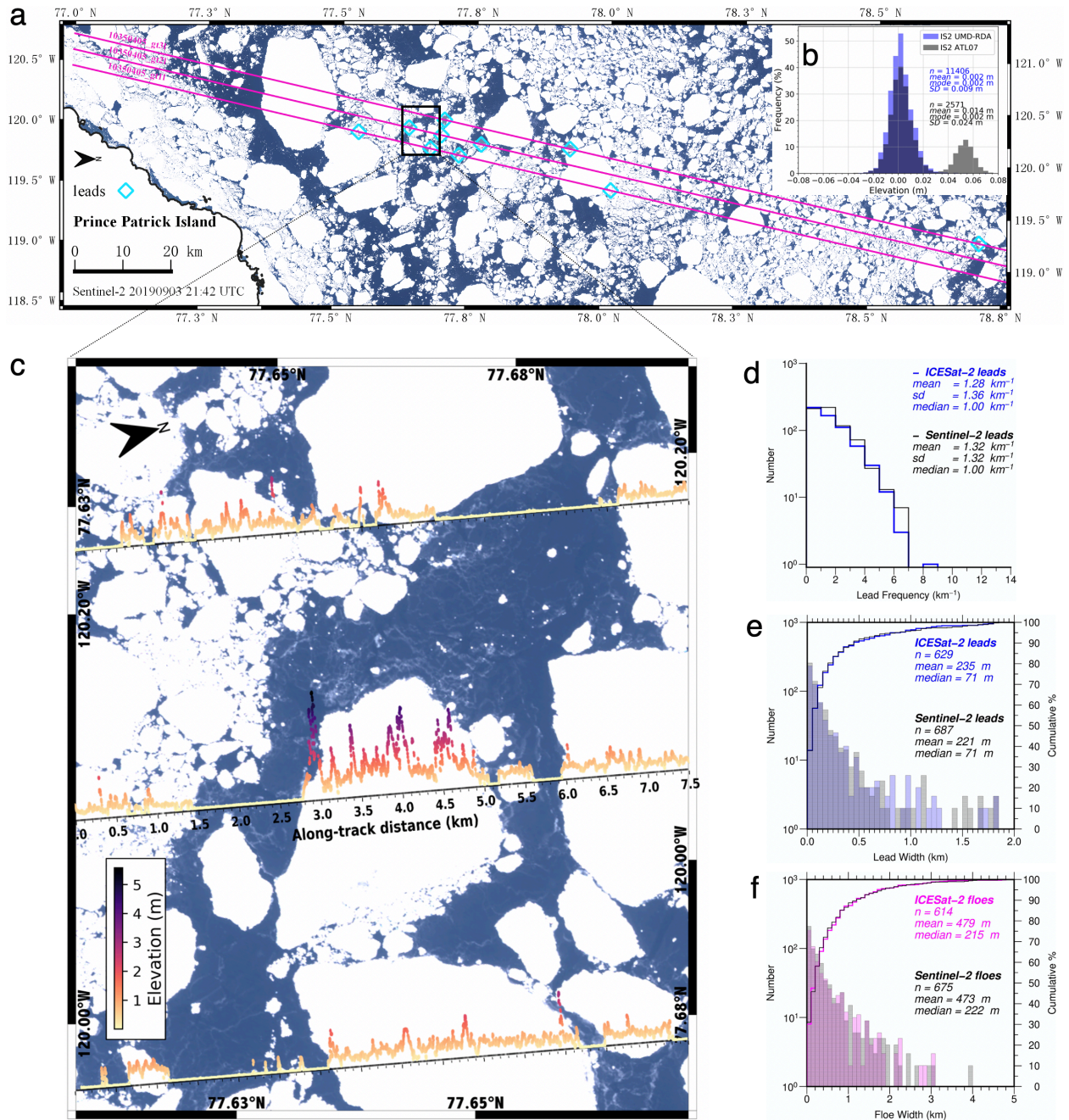
354



355

356 **Figure 2.** Detection of sea ice melt ponds with ICESat-2. (a) ATL03 photon heights (gray),  
 357 ATL07 surface height (cyan), and UMD-MPA-derived melt pond (MP) surface (black) and  
 358 bottom (magenta) elevations. (b) Validation of melt signals in a coincident Sentinel-2 MSI image  
 359 collected June 22, 2019 at 19:50:26 UTC, 37 minutes prior to the ICESat-2 overpass on RGT  
 360 13070304. (c) Depth distribution for ponds MP1-10 shown in (a).

361



362

363 **Figure 3.** Arctic floe size distribution and lead frequency at the end of summer. (a) Sea ice  
 364 conditions in the Canada Basin (region D, figure 1) on September 3, 2019 as observed by  
 365 Sentinel-2. Coincident data obtained along a ~200 km-long ICESat-2 transect (magenta lines).  
 366 (b) Elevation derived from the UMD-RDA (blue) and ATL07 (gray) ICESat-2 products over ten  
 367 leads (cyan diamonds, a). (c) 7.5 km-long transect of sea ice elevation within highlighted region  
 368 (black box, a), derived from the UMD-RDA ICESat-2 product, overlaid on a coincident Sentinel-  
 369 2 MSI image. Elapsed time between satellite acquisitions was 11 minutes. (d) Lead frequency

370 derived from ICESat-2 (blue) and Sentinel-2 (black) along the three strong beams of  
371 RGT10350405 shown in (a). (e) Lead width statistics derived from ICESat-2 (blue) and Sentinel-  
372 2 (black). (f) Floe size statistics derived from ICESat-2 (magenta) and Sentinel-2 (black).

373

## 374 **References**

375

376 Arntsen A. E., Song A. J., Perovich D. K. & Richter-Menge J. A. (2015). Observations of the  
377 summer breakup of an Arctic sea ice cover. *Geophys Res Lett*, 42, 8057–  
378 8063, <http://dx.doi.org/10.1002/2015GL065224>

379

380 Brunt, K. M., Neumann, T. A., & Smith, B. E. (2019). Assessment of ICESat-2 ice sheet surface  
381 heights, based on comparisons over the interior of the Antarctic ice sheet. *Geophysical Research*  
382 *Letters*, 46, 13,072–13,078. <https://doi.org/10.1029/2019GL084886>

383

384 Buckley, E. M., Farrell, S. L., Duncan, K., Connor, L. N., Kuhn, J. M., & Dominguez, R. T.  
385 (2020). Classification of sea ice summer melt features in high-resolution IceBridge imagery. *J.*  
386 *Geophys. Res.*, 125, e2019JC015738. <https://doi.org/10.1029/2019JC015738>

387

388 Curry, J. A., Schramm, J. L., & Ebert, E. E. (1995). Sea ice-albedo climate feedback mechanism.  
389 *Journal of Climate*, 8(2), 240-247.

390

391 Duncan, K., Farrell, S. L., Connor, L. N., Richter-Menge, J. & Dominguez, R. (2018). High-  
392 Resolution Airborne Observations of Sea Ice Pressure-Ridge Sail Height. *Annals of Glaciology*,  
393 59(76pt2), 137-147. <https://doi.org/10.1017/aog.2018.2>

394

395 Duncan, K., Farrell, S. L., Hutchings, J., & Richter-Menge, J. (2020). Late Winter Observations  
396 of Sea Ice Pressure Ridge Sail Height. *IEEE Geoscience & Remote Sensing Lett.*  
397 <https://doi.org/10.1109/LGRS.2020.3004724>

398

- 399 Eicken, H., Grenfell, T. C., Perovich, D. K., Richter-Menge, J. A. & Frey, K. (2004). Hydraulic  
400 controls of summer Arctic pack ice albedo. *J. Geophys. Res.*, *109*, C08007.  
401 <https://doi.org/10.1029/2003JC001989>  
402
- 403 Farrell, S. L., Brunt, K. M., Ruth, J. M., Kuhn, J. M., Connor, L. N., & Walsh, K. M. (2015). Sea  
404 Ice Freeboard Retrieval using Digital Photon-counting Laser Altimetry. *Ann. Glaciol.*, *56*(69),  
405 167–174. <https://doi.org/10.3189/2015AoG69A686>  
406
- 407 Farrell, S. L., Laxon, S. W., McAdoo, D. C., Yi, D., & Zwally, H. J. (2009). Five years of Arctic  
408 sea ice freeboard measurements from the Ice, Cloud and land elevation Satellite. *J. Geophys.*  
409 *Res.*, *114*, C04008. <https://doi.org/10.1029/2008JC005074>  
410
- 411 Farrell, S. L., Markus, T., Kwok, R. & Connor, L. (2011). Laser Altimetry Sampling Strategies  
412 over Sea Ice. *Annals Glaciol.*, *52*(57), 69-76. <https://doi.org/10.3189/172756411795931660>  
413
- 414 Horvat, C., & Tziperman, E. (2017). The evolution of scaling laws in the sea ice floe size  
415 distribution. *J. Geophys. Res. Oceans*, *122*, 7630–7650. <https://doi.org/10.1002/2016JC012573>  
416
- 417 Hunke, E. C., Hebert, D. A., & Lecomte, O. (2013). Level-ice melt ponds in the Los Alamos sea  
418 ice model, CICE. *Ocean Modelling*, *71*, 26-42.  
419
- 420 Hwang, B., Ren, J., McCormack, S., Berry, C., Ayed, I. B., Graber, H. C., & Aptoula, E. (2017).  
421 A practical algorithm for the retrieval of floe size distribution of Arctic sea ice from high-  
422 resolution satellite Synthetic Aperture Radar imagery. *Elem Sci Anth*, *5*.  
423
- 424 Kwok, R., G. Cunningham, T. Markus, D. Hancock, J. H. Morison, S. P. Palm, S. L. Farrell, A.  
425 Ivanoff, J. Wimert, & the ICESat-2 Science Team. (2019a). ATLAS/ICESat-2 L3A Sea Ice  
426 Height, Version 2. Boulder, Colorado USA. NSIDC: National Snow and Ice Data Center.  
427 <https://doi.org/10.5067/ATLAS/ATL07.002>  
428

- 429 Kwok, R., Kacimi, S., Markus, T., Kurtz, N. T., Studinger, M., Sonntag, J. G., et al. (2019b).  
430 ICESat-2 surface height and sea ice freeboard assessed with ATM lidar acquisitions from  
431 Operation IceBridge. *Geophysical Research Letters*, 46. <https://doi.org/10.1029/2019GL084976>  
432
- 433 Kwok, R., Markus, T., Kurtz, N. T., Petty, A. A., Neumann, T. A., Farrell, S. L., Cunningham,  
434 G. F., Hancock, D. W., Ivanoff, A., & Wimert, J. (2019c), Surface height and sea ice freeboard  
435 of the Arctic Ocean from ICESat-2: Characteristics and early results. *J. Geophys. Res.*, 124.  
436 <https://doi.org/10.1029/2019JC015486>  
437
- 438 Kwok, R., Zwally, H. J., & Yi, D. (2004). ICESat observations of Arctic sea ice: A first look.  
439 *Geophys. Res. Lett.*, 31, L16401. <https://doi.org/10.1029/2004GL020309>  
440
- 441 Laxon, S. W., Giles, K. A., Ridout, A. L., Wingham, D. J., Willatt, R., Cullen, R., Kwok, R.,  
442 Schweiger, A., Zhang, J., Haas, C., Hendricks, S., Krishfield, R., Kurtz, N., Farrell, S. L., &  
443 Davidson, M. (2013). CryoSat Estimates of Arctic Sea Ice Volume. *Geophys. Res. Lett.*, 40(4),  
444 732-737. <https://doi.org/10.1002/grl.50193>  
445
- 446 Magruder, L., Neumann, T., Fricker, H., Farrell, S., Brunt, K., Gardner, A., ... & Kurtz, N.  
447 (2019). New Earth orbiter provides a sharper look at a changing planet. *Eos, Transactions*  
448 *American Geophysical Union*, 100. <https://doi.org/10.1029/2019EO133233>  
449
- 450 Markus, T., Neumann, T., Martino, A., Abdalati, W., Brunt, K., Csatho, B., Farrell, S. et al.  
451 (2017). The Ice, Cloud, and land Elevation Satellite-2 (ICESat-2): Science requirements,  
452 concept, and implementation. *Rem. Sens. Environ.*, 190, 260-273.  
453 <https://doi.org/10.1016/j.rse.2016.12.029>  
454
- 455 Neumann, T. A., A. Brenner, D. Hancock, J. Robbins, J. Saba, K. Harbeck, A. Gibbons, J. Lee,  
456 S. B. Luthcke, T. Rebold, et al. (2020). ATLAS/ICESat-2 L2A Global Geolocated Photon Data,  
457 Version 3. Boulder, Colorado USA. NSIDC: National Snow and Ice Data Center.  
458 <https://doi.org/10.5067/ATLAS/ATL03.003>  
459

- 460 Parrish, C. E., Magruder, L. A., Neuenschwander, A. L., Forfinski-Sarkozi, N., Alonzo, M., &  
461 Jasinski, M. (2019). Validation of ICESat-2 ATLAS Bathymetry and Analysis of ATLAS's  
462 Bathymetric Mapping Performance. *Remote Sensing*, *11*(14), 1634.
- 463
- 464 Perovich, D. K., Grenfell, T.C., Richter-Menge, J. A., Light, B., Tucker III, W. B., & Eicken, H.  
465 (2003). Thin and thinner: Sea ice mass balance measurements during SHEBA. *J. Geophys. Res.*,  
466 *108*(C3), 8050. <https://doi.org/10.1029/2001JC001079>
- 467
- 468 Perovich, D., Meier, W., Tschudi, M., Farrell, S., Hendricks, S., Gerland, S., Kaleschke, L.,  
469 Ricker, R., Tian-Kunze, X., Webster, M., & Wood, K. (2019). Sea ice. In *Arctic Report Card*  
470 *2019*, J. Richter-Menge, M. L. Druckenmiller, and M. Jeffries (Eds.).  
471 <http://www.arctic.noaa.gov/Report-Card>
- 472
- 473 Perovich, D. K., & Polashenski, C. (2012). Albedo evolution of seasonal Arctic sea ice.  
474 *Geophys. Res. Lett.*, *39*, L08501. <https://doi.org/10.1029/2012GL051432>
- 475
- 476 Perovich, D. K., & Richter-Menge, J. A. (2015). Regional variability in sea ice melt in a  
477 changing Arctic. *Phil. Trans. R. Soc. A*, *373*, 20140165. <http://doi.org/10.1098/rsta.2014.0165>
- 478
- 479 Perovich, D. K., Tucker III, W. B., & Ligett, K. A. (2002). Aerial observations of the evolution  
480 of ice surface conditions during summer. *J. Geophys. Res.*, *107*(C10), 8048.  
481 <https://doi.org/10.1029/2000JC000449>
- 482
- 483 Roach, L. A., Horvat, C., Dean, S. M., & Bitz, C. M. (2018). An emergent sea ice floe size  
484 distribution in a global coupled ocean-sea ice model. *Journal of Geophysical Research: Oceans*,  
485 *123*, 4322–4337. <https://doi.org/10.1029/2017JC013692>
- 486
- 487 Richter-Menge, J., Osborne, E., Druckenmiller, M., & Jeffries, M. O. (Eds.). (2019). The Arctic.  
488 In *State of the Climate in 2018*, *Bull. Amer. Meteor. Soc.*, *100* (9), S141–S168.  
489 <https://doi.org/10.1175/2019BAMSSStateoftheClimate.1>
- 490

- 491 Scott, F., & Feltham, D. L. (2010). A model of the three-dimensional evolution of Arctic melt  
492 ponds on first-year and multiyear sea ice. *J. Geophys. Res.*, *115*, C12064,  
493 <https://doi.org/10.1029/2010JC006156>  
494
- 495 Shepherd, A., Fricker, H. A., & Farrell, S. L. (2018). Trends and Connections Across the  
496 Antarctic Cryosphere. *Nature*, *558*, 223-232, <https://doi.org/10.1038/s41586-018-0171-6>  
497
- 498 Turner, J. & Comiso, J. (2017). Solve Antarctica's sea-ice puzzle. *Nature*, *547*(7663), 275-277.  
499
- 500 Vose, R.S., Applequist, S., Durre, I., Menne, M.J., Williams, C.N., Fenimore, C., Gleason, K. &  
501 Arndt, D. (2014). Improved Historical Temperature and Precipitation Time Series For U.S.  
502 Climate Divisions. *Journal of Applied Meteorology and Climatology*.  
503 <http://dx.doi.org/10.1175/JAMC-D-13-0248.1>  
504
- 505 Wingham, D. J., Francis, C. R., Baker, S., Bouzinac, C., Brockley, D., Cullen, R., de Chateau-  
506 Thierry, P., Laxon, S. W., Mallow, U., Mavrocordatos, C. and Phalippou, L. (2006). CryoSat: A  
507 mission to determine the fluctuations in Earth's land and marine ice fields. *Advances in Space*  
508 *Research*, *37*(4), 841-871. <http://dx.doi.org/10.1016/j.asr.2005.07.027>  
509
- 510 World Meteorological Organization. (1970). Sea ice nomenclature: Terminology, Codes and  
511 Illustrated Glossary, WMO/OMM/ BMO 259, TP 145, World Meteorological Organization,  
512 Geneva.  
513 [https://www.jcomm.info/components/com\\_oa/oa.php?task=download&id=27226&version=March](https://www.jcomm.info/components/com_oa/oa.php?task=download&id=27226&version=March%202014&lang=1&format=1)  
514 [h 2014&lang=1&format=1](https://www.jcomm.info/components/com_oa/oa.php?task=download&id=27226&version=March%202014&lang=1&format=1)  
515
- 516 Zwally, H. J., Schutz, B., Abdalati, W., Abshire, J., Bentley, C., Brenner, A., ... & Herring, T.  
517 (2002). ICESat's laser measurements of polar ice, atmosphere, ocean, and land. *Journal of*  
518 *Geodynamics*, *34*(3-4), 405-445.  
519